CHAPTER 5
PROPOSED THRUST FAILURE MECHANISM FOR SLOPE STABILITY ANALYSES IN COMPLEX GEOTECHNICAL CONDITIONS

5.1 SUMMARY

In this chapter all the results of the observations, modelling, and fracture analysis come together to develop a thrust failure mechanism in which the failures in the coal mine are explained as completely as possible. The proposed mechanism is a blocky-type failure mechanism, and the blocks are defined by internal shear failures that link up with fracture formation along the shale – middle coal seam contact. These proposals agree very well with Boyd's (1983) observations on the formation of an active block boundary.

5.2 INTRODUCTION

The proposed failure mechanism is based on the polygonal failure surfaces theory by Kovari and Fritz (1978), Boyd's observations (1983 – Figure 1.1), Stead and Scoble (1983 – Figure 1.2), failure modes from Figures 1.4 and 1.5 and the shear stress analyses discussed in this chapter. From the literature it is known that sliding usually takes place on curved surfaces that can be modelled by concave-up polygonally–shaped surfaces. For such cases, Janbu (1954) and Morgenstern and Price (1967) have suggested practical methods of computation, according to which the unstable earth- or rock-mass is divided up into vertical strips or slices. The Kovari and Fritz (1978)

polygonal failure surfaces theory is based on certain assumptions regarding the distribution and slope of the internal contact forces, as well as the hypothesis of limit equilibrium. Their method is based upon the physical requirement that sliding on a polygonal surface is only possible kinematically if a sufficient number of internal shear surfaces can develop. For the sake of simplification, only continuous shear surfaces starting from the intersection lines of the polygon-sliding surface are assumed. Thus, as shown in Figure 5.1, the slide of a mass on three surfaces must be accompanied by at least two internal shear surfaces. For n external sliding surfaces ($n-1$) such interfaces are required.

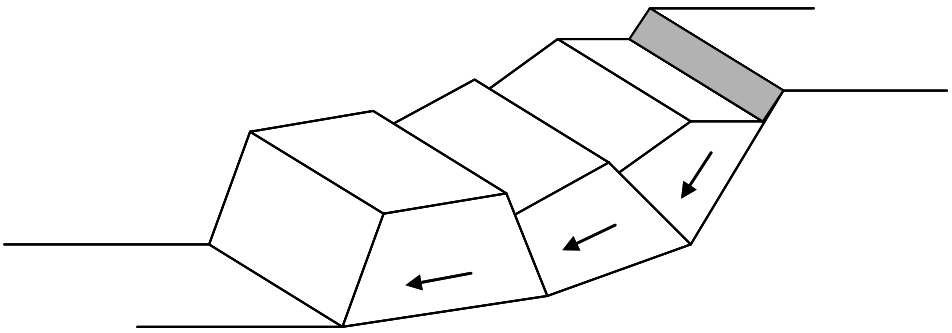

Figure 5.1
Kinematics of a slope failure for a polygonal sliding surface (after Kovari and Fritz, 1978)

The Kovari and Fritz (1978) method rests upon the following basic assumptions:

1. The blocks comprising the rock mass are each considered to be rigid.
2. The directions of the internal shear surfaces are known.

3. On the internal and external sliding surfaces (at the condition of limit equilibrium) the Mohr-Coulomb failure criterion applies, and no tensile strength is permitted. The strength parameters may be allocated different values on each sliding surface.

The direction of the internal shear surfaces is chosen from case to case on the basis of a careful investigation of the structure of the potentially sliding mass. However, for highly jointed rock, the directions of the internal slip surfaces are found by the condition of a minimum safety factor for the system. In an investigation of the stability of an earth dam, Sultan and Seed (1967) used a similar criterion.

The Kovari and Fritz (1978) method does not take into account the existence of complex geotechnical structure within the slope. It also ignores the formation of a tensile fracture behind the slope crest, which is a common feature in competent rock slopes. In their method, the internal failure surfaces are determined by careful field observation, which has an element of subjectivity introduced by observer experience.

The proposed thrust failure mechanism simplifies Kovari and Fritz's (1978) method by using only three failure surfaces as the investigated slope profile is divided into two block types: so-called "passive" and "active" blocks. The proposed method also takes into account the tensile fracture behind the crest of the slope.

5.3 DETERMINING SHEAR FAILURE ZONE DIRECTIONS IN THE SLOPE

Fracture development in rock is complex and remains poorly understood. In layered sedimentary rocks, opening-mode fractures have been observed to abut against bedding contacts (Baer, 1991; Narr and Suppe, 1991; Gross et al., 1995; Becker and Gross, 1996; Ji and Saruwatari, 1998), cross through contacts (Becker and Gross, 1996), and jog or step-over at bedding contacts (Helgeson and Aydin, 1991). Fracture termination at frequent bedding contacts can produce highly tortuous fracture paths in sediments (Tsang, 1984). By contrast, fractures that propagate straight through bedding contacts provide well-connected pathways. A potential intermediate case is a fracture that jogs or steps over a few centimetres at bedding contacts (Helgeson and Aydin, 1991). Although these three types of fracture intersection with bedding are easily recognised in the field, the mechanisms that control the development of one as opposed to another type are not yet well understood. Insight into controlling mechanisms and parameters could aid the prediction of subsurface fracture propagation.

Even in solid rock material (where jointing and other structures are insignificant), shear failure remains a complex process resulting in complex fracture structures. A common terminology for brittle shear fractures in rock is introduced below (adapted from Riedel, 1929, Sylvester, 1988, and Vermeer and de Borst, 1984) and shown in Figure 5.2. Riedel’s (1929) paper is not available, and his work is completely unknown in solid mechanics, while it is widely

referenced in geology. The reproductions of his interpretations in Sylvester (1988) and McKinnon and de la Barra (1998) are probably misleading because there is no mechanistic description of how the various fractures develop. Riedel's work should be revisited from a solid mechanics point of view, because it provides a good starting point for the interpretation, from a stress and deformation point of view, of small and large faults in rockmasses.

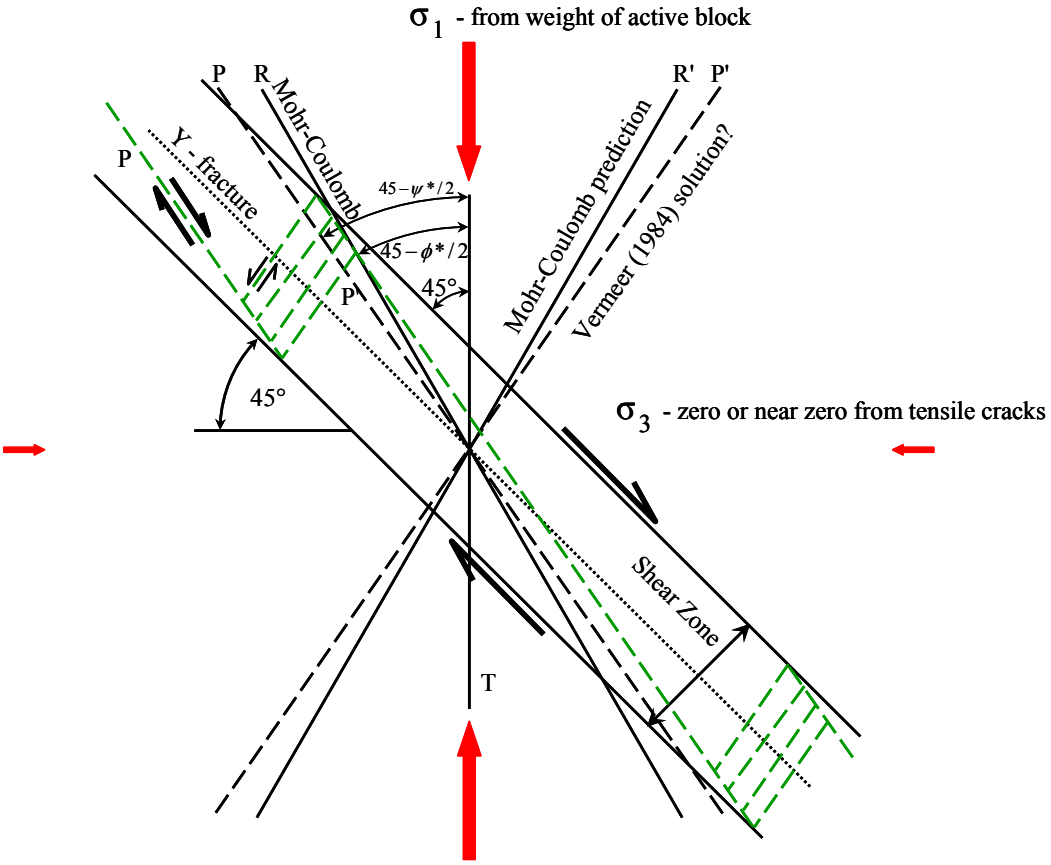

Figure 5.2

The Riedel (1929) Shear Fracture Model in green showing typical orientation relative to the major principal stress and direction of shearing

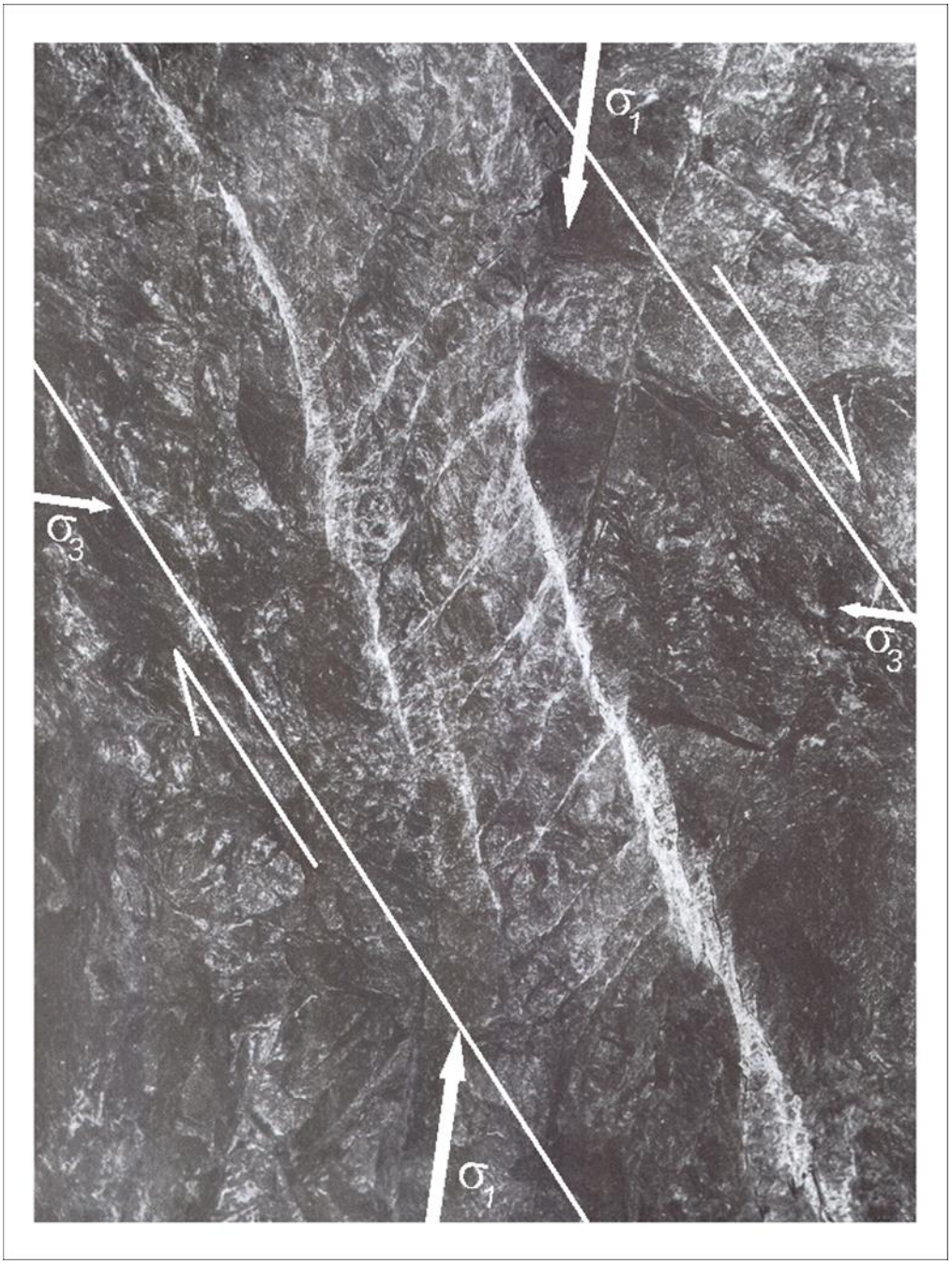

Picture 5.1

Example of a shear fracture in brittle rock in a deep level gold mine showing Riedel Structures (after Ortlepp, 1997)

The location chosen in the slope for the stress state shown is just below the modelled horizontal tensile zone, where the horizontal stresses will be small. There is no mechanistic reason for this excepting that this point has the maximum isolated block weight above it (the block is assumed to be defined by two or more tensile fractures behind the slope crest) and this should be a favourable point for the origin of shearing, where the horizontal stresses are low. The shearing fractures are also assumed to have the complexity of shearing seen in all geological materials, i.e. along faults, in mines, and in the laboratory. Since Riedel (1929) presented his shearing model, it has been widely accepted and has again and again been demonstrated to be a reliable guide for the interpretation of shear along all types of geological features.

Riedel fractures, R and R', form a conjugate set about the major principal stress direction, and are here drawn using Vermeer and de Borst's (1984) notation in which $\phi*$ is the mobilised angle of internal friction. Tension fractures, T, form in the direction of major principal stress, P fractures form symmetrically to the R fractures with respect to the shear direction (these are conjectured to be Vermeer and de Borst's 1984 solution, see equation 5.1 below), while Y fractures are those that lie parallel to the direction of applied shear displacement. All of these fracture types have been observed in nature (Tchalenko and Ambraseys, 1970; Gammond, 1983 and Ortlepp, 1997 – Picture 5.1). McKinnon and de la Barra (1998) have modelled the shear failures, and on the basis of small-strain Mohr-Coulomb theory they have found that it is not possible to

explain the formation of primary P or Y fractures. It now appears that Vermeer and de Borst's (1984) solution for non-associated flow may explain the P fractures, but this is beyond the scope of this thesis. Bartlett et al. (1981) report that all the fracture types illustrated by Riedel (1929) have been reproduced in various laboratory tests.

As mentioned above, the orientation of R and R' fractures can be deduced from the Mohr circle. For a rock with strength defined by cohesion **c** and friction angle ϕ, fracture occurs on planes oriented at $\pm(45-\phi/2)$ from σ_1 as shown in Figure 5.2. Depending on the amount of confining pressure, σ_3, tension fractures T may occur parallel to the σ_1 direction. Using plasticity theory, Vermeer (1990) have shown that for a hardening modulus h_c of zero in non-associated flow, there are two possible solutions for θ, namely:

$$\frac{\pi}{4}-\left(\frac{\phi^{*}+\psi^{*}}{4}\right)<\theta<\frac{\pi}{4}-\frac{\phi^{*}}{2} \qquad (5.1)$$

where ψ^* and ϕ^* are the *mobilised* angle of dilation and *mobilised* angle of internal friction i.e. they are some function of the strain in the material (Vermeer and de Borst, 1984). Combining the results of Riedel (1929) and Vermeer and de Borst (1984), we know that plastic shear flow in the slope must be non-associated, hence $\phi^* \neq \psi^*$, and by implication in Figure 5.2 and Vermeer (1990), that $\phi^* > \psi^*$.

The purpose of presenting all this detail is to recognise that the formation of shear zones in the slope will be complex, just as they are in any

geological material. However, Riedel's (1929) observation that the shear fracture structure is complex, contrasts with the simple observation that the *shear zone orientation* is simple, i.e. it can be assumed to lie parallel with the direction of the largest shear stress in the slope. Shear bands or fractures, however, need not occur at only one specific angle, but could occur over a range of angles in relation to the maximum principal stress direction together with the effects of anisotropy in the shale (e.g. Jaeger and Cook, 1979). Note that only one possible Riedel Shear Structure is drawn in green in Figure 5.2 in which the conjectured Vermeer and de Borst (1984) dilation solution has been applied. The other possible Mohr-Coulomb alternative is not shown for purposes of keeping the drawing clear.

To analyse the inclination of the principal stress directions and consequently to identify the shear failure zones, that may develop in the slope, three horizontal profile lines were defined at 15, 20 and 25m below surface (Figure 5.3). These profile lines were applied to the discussed in Chapters 2 and 3 scenarios of layer inclination (5^0 and 15^0) in homogeneous sandstone slope profile and slope profiles with embedded shale layer thickness from 2m to 12m on 2m intervals. These profile lines provide the reader with reference lines in Figures 5.4 and 5.5. The window chosen has to be relatively small to render the principal stress tensor representations clearly, hence the position of the window in relation to the slope profile shown in Figure 5.3.

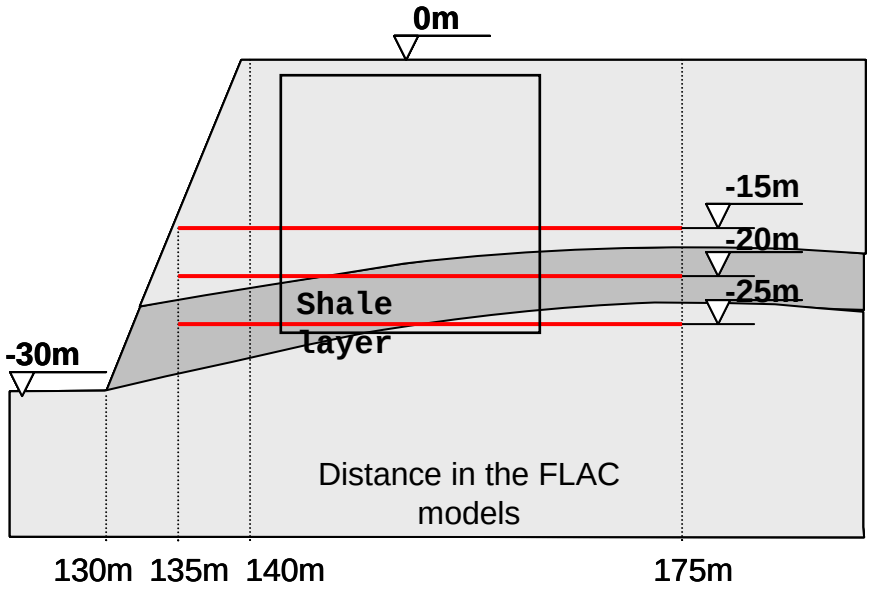

Figure 5.3

Profile line positions (marked with red) in the slope profile together with the position of the slope profile elements in the FLAC models

Figures 5.4 and 5.5 show the principal stress distributions for 6m and 8m thick shale layers respectively and 15^0 layer inclination in the models. Similar results were obtained for all the cases studied with steeper layer inclination angle in the model. The principal stress direction inclination angles of all investigated scenarios can be seen in Figures A3.10 - A3.13, Appendix 3. On these figures it can be seen that only the profiles with steeper layer (15^0 inclination angle) and 6m, 8m and 10m layer thickness have very well defined zones, along the profile line at 20m depth, with horizontal orientation of the principal stress direction inclination angle. For better presentation, these zones are tabulate in Table 5.1.

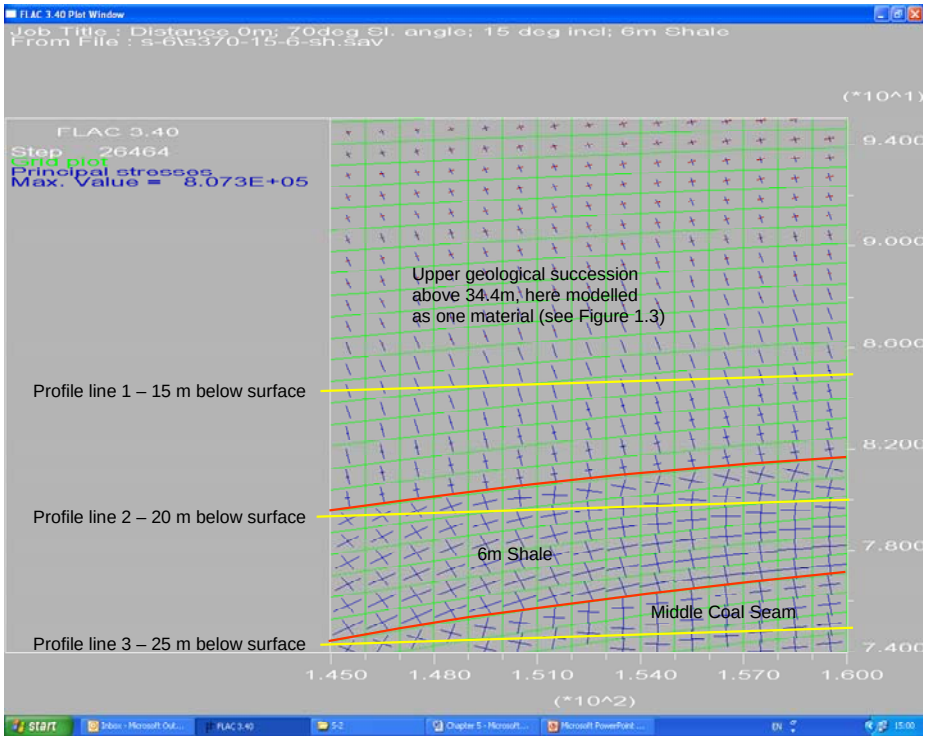

Figure 5.4

Maximum principal stress directions and inclinations in 6m thick shale and surrounding strata

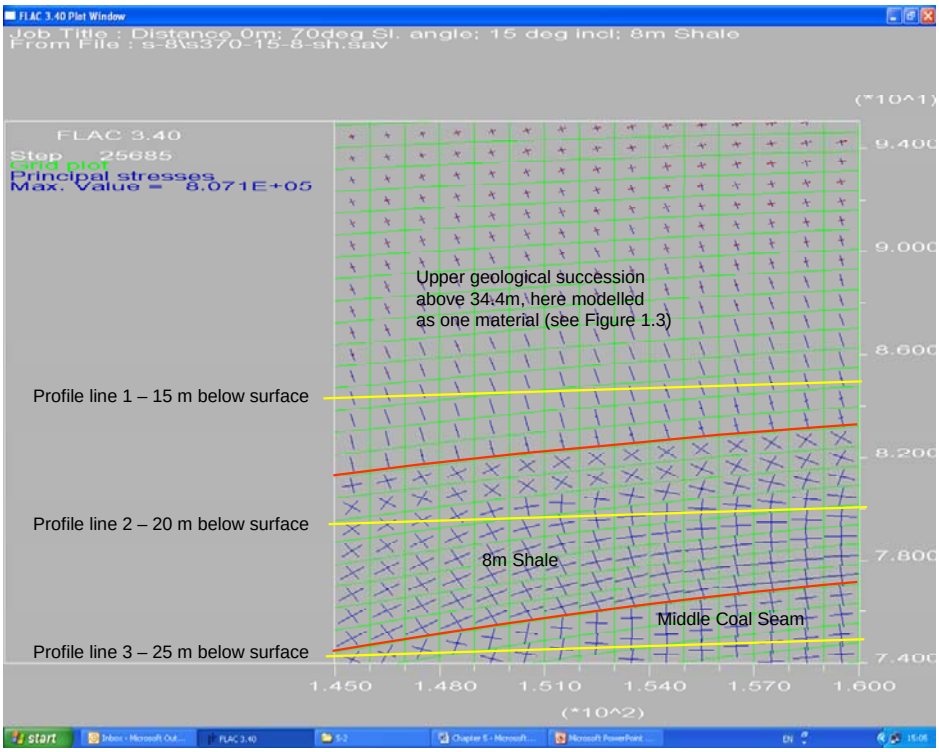

Figure 5.5

Maximum principal stress directions and inclinations in 8m thick shale and surrounding strata

Table 5.1 Points with almost horizontal principal stress direction along the profile line at 20m depth and different shale layer thickness in the slope profile

Shale layer thickness in the model (m)	Distance from the left model boundary (m)	
	First point	Second point
6	150	155
8	150	157
10	151	158

The slope profile with 15^0 layer inclination and thickest embedded shale layer (12m of thickness) exhibits only one zone on 157m from the model length at 20m depth.

Figure 5.6 shows the most likely averaged shear zone directions resulting from the principal stress distributions in Figures 5.4 and 5.5. Parts of the shear zone may even be vertical, given the inclination of the principal stress tensor near the top contact of the shale. In the solution given, the author has assumed that the shear zones are inclined at 45° to the horizontal, and that they are approximated by straight lines.

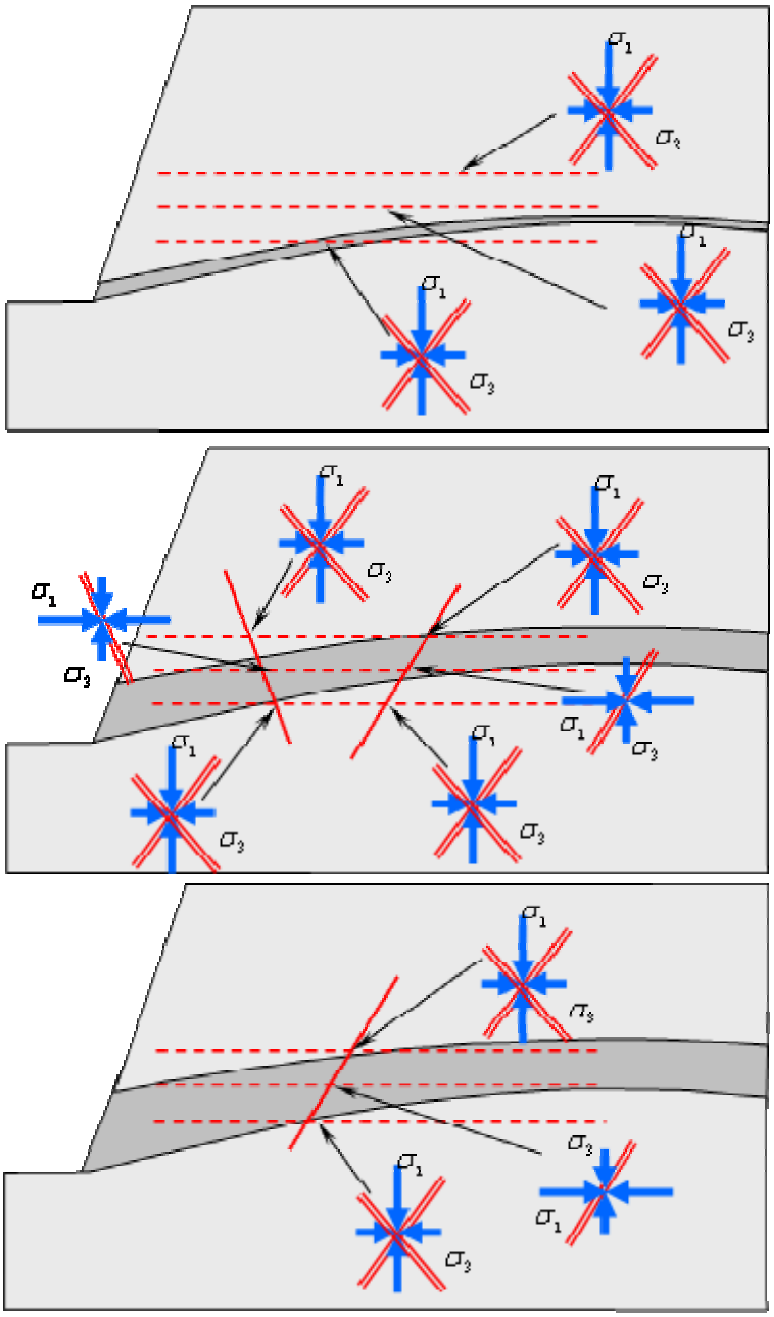

Figure 5.6

Conjectured shear zone orientations in slope profile with different shale thicknesses

There are two arguments that support the conjecture that the shear zones are angled at 45° to the horizontal:

- The FLAC model cannot reproduce failure and all its implications on the stress state in the slope;
- The principal stress orientations in Figures 5.4 and 5.5 will change with the development of the shear fractures, and will tend towards the vertical because of the block's weight.

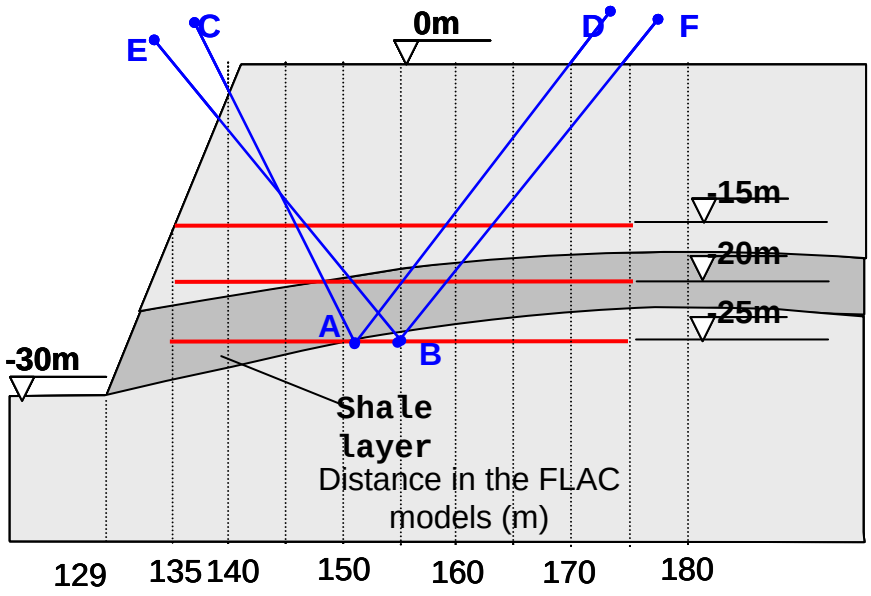

Figure 5.7

Shear failure lines (marked with blue) due to the inclinations of the principal stress direction inclination angles in Figures 5.4 – 5.6

The lines in Figure 5.7 define probable shear surfaces bounding two active blocks. The lines "*CAD*" represent lock boundaries for 6m thick shale, and lines "*EBF*" represent potential shear boundaries for slopes with 10m-thick shale. The differences between the two are not considered particularly significant, especially in the light of our approximate knowledge of slope failure mechanisms and in-situ stress states, hence the author assumes shear zones inclined at 45° to the horizontal.

5.4 ASSUMPTIONS REGARDING THE PROPOSED THRUST FAILURE MECHANISM

The proposed failure mechanism is based on the findings, definitions and assumptions set out in Chapter 4 and the previous paragraph 5.3.

1. The slope profile can be divided into two blocks – the passive and active block (after Boyd, 1983). See Figures 1.1 and 5.1.

This assumption is based on the Kovari and Fritz (1978) polygonal failure surface theory. The existence of the active block is confirmed by field observations. The modelling supports this observation by suggesting that the ground behind the slope crest tends to "slump" downwards by almost a millimetre because of the reduction of horizontal stresses because of the presence of the slope (see Figure 5.8).

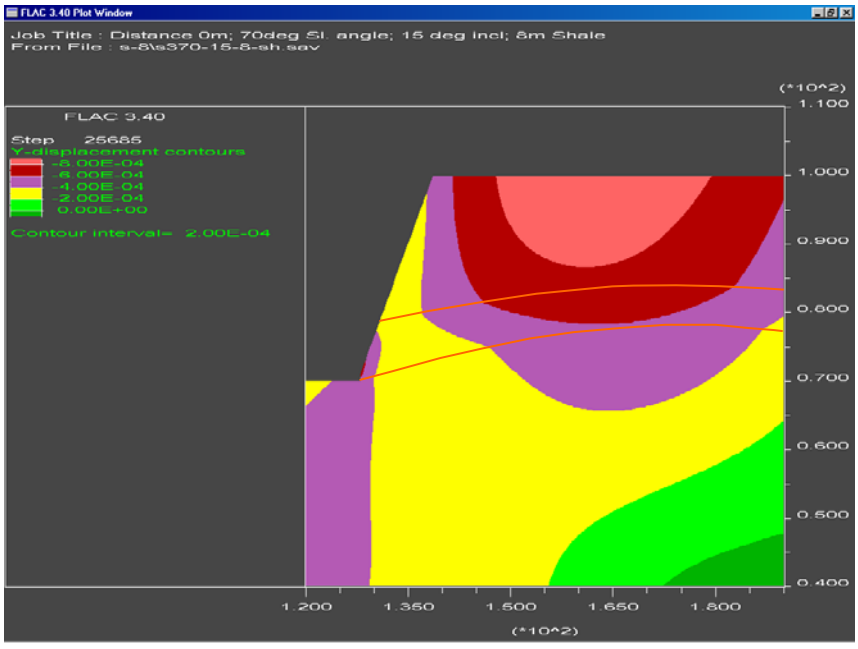

Figure 5.8

Vertical displacement contours in slope containing an 8m-thick shale layer (marked with a red line)

2. Failure takes place on the bottom contact surface of the shale with the middle coal seam, and this surface is always exposed at the toe of the slope (the mining method is to remove overburden in two stages to the top and middle coal seams respectively, and thereafter to mine the exposed coal).

This assumption is based on the site observations of the failure surface profiles (see Figures 1.1 and 1.8) and the Kovari and Fritz (1978) polygonal failure surfaces theory. As was discussed in Chapter 4, the passive block has frictional resistance along the contact surface in the area where $|\Delta\sigma_N| > |\Delta\sigma_N^P|$ and cohesive resistance when $|\Delta\sigma_N| < |\Delta\sigma_N^P|$.

3. The tensile fracture depth is equal to the depth of the induced horizontal tensile stress component.

In a series of very detailed model studies on slope failures, Barton (1971) found that the tension crack behind the slope crest was generated by small movements within the rock mass, and that it appeared after slope excavation. Although these individual movements were very small, their cumulative effect was a significant displacement of the slope surface - sufficient to cause separation of material behind the slope crest and to form tension cracks. In Section 3.5 we estimated the depth of the tensile zone above the undulated strata formation after the slope had been cut, and we assume that tensile fracture depth is equal to the depth of

the horizontal tensile stress zone, here estimated to be 10 to 12m deep (see Figure 3.7).

4. The vertical active block boundaries are defined by the vertical tensile cracks.

If a tensile zone (under different geotechnical conditions) develops in the slope profile as a result of the slope excavation, the active block sides are formed by vertical tensile fractures.

5. The active block stretches from the crest of the slope back toward the solid.

The purpose of this assumption is to determine the possibility of blocky-type failure as close as possible to the plane of weakness formed by frictional zone. This assumption is based on Figures 5.4–5.7 and A3.16–A3.19.

6. Below the tensile zone, the active block boundaries fail by shear zones formed at an angle of 45° to the horizontal, to form a wedge at the base with an angle of 90°.

The shear failure is triggered by the active block weight once its upper portion has become isolated from the rest of the slope by the vertical tensile fractures.

7. Inter-block forces are not taken into account because the failure mode consists of two blocks only. The vectors of their side forces are assumed

to be equal and opposite on opposite sides of the failure zones for equilibrium.

Instead of inter-block forces, reaction forces acting from the passive block to the active block are taken into account.

8. The shale and other rocks in the slope have low porosities (3-4%), but it is assumed that the pores are hydraulically connected.

This assumption is based on the widely accepted zero pore-water pressure at the toe of the slope (Hoek and Bray, 1981 and Hoek, 1986).

9. The analysis can be undertaken with reasonable accuracy in two dimensions, assuming unit length out-of-plane.

The proposed active and passive blocks appear in Figure 5.9 below.

5.5 PROPOSED THRUST FAILURE MECHANISM

When the artificial cut is made, fracture propagation starts as a result of rock relaxation. At this time, the vertical tensile fractures at ground surface and the possible tensile fracture (if $|\Delta\sigma_N| > |\sigma_N^P|$) at the toe of the slope along the shale-middle coal seam contact surface are formed. After their formation, the slope profile fails by shear along unbroken ligaments, as we assumed in Section 5.4. Once these fractures have formed, continued slope stability is seen to be only a

consequence of the balance of forces existing in the profile.

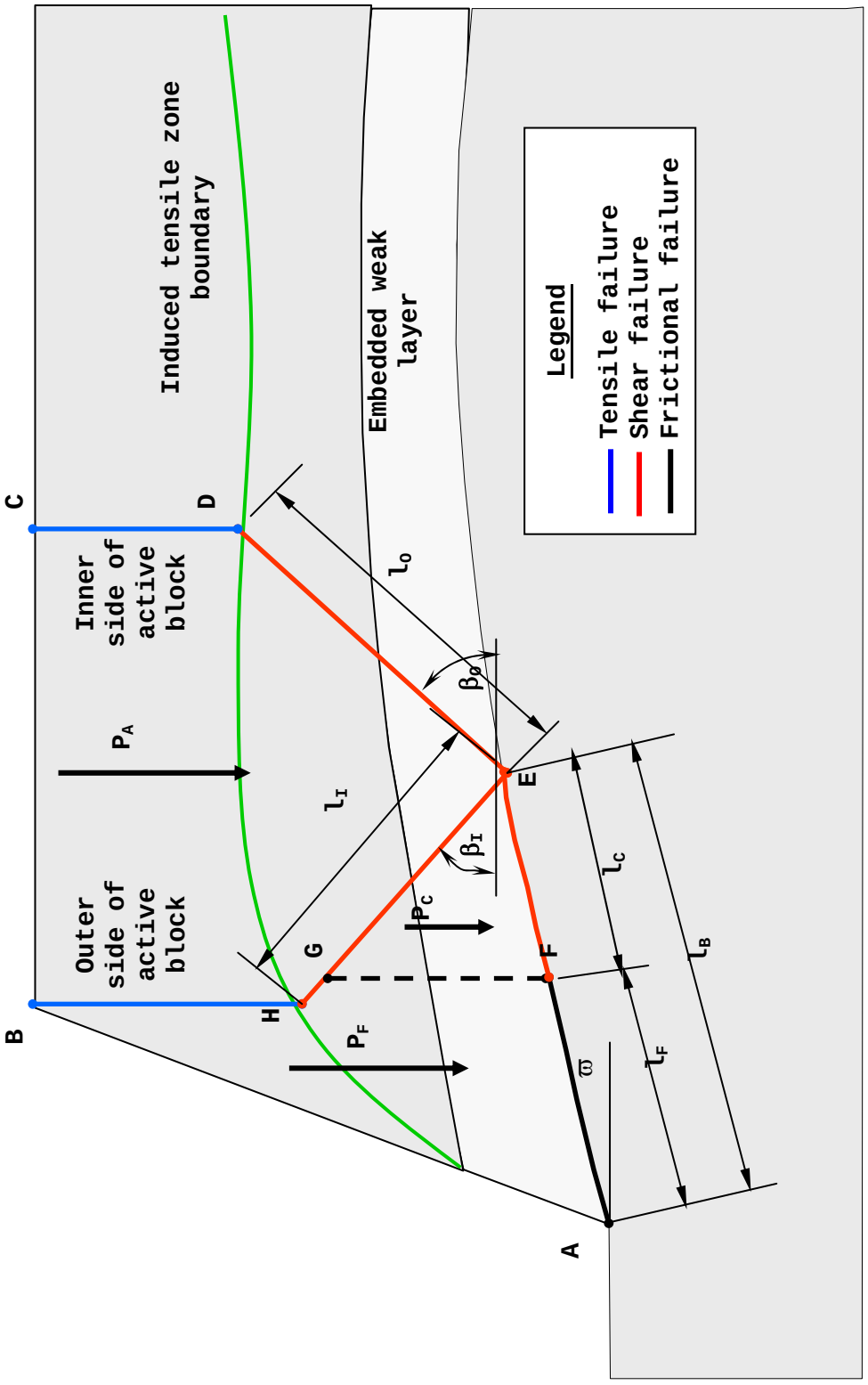

Figure 5.9 Active (B,C,D,E,G,H) and the passive (A,B,H,G,E,F) block formation with indicated lengths of the failure types at the boundary of the blocks

It is also important to recognise that this analysis considers only force equilibrium and assumes that all forces pass through the block centroids. In other words, moment equilibrium is not considered in this model because observations of the failures at the mine did not reveal any significant rotational motion in the failures.

Figure 5.9 indicates the failure length and type taken into account for the purpose of the slope stability calculations. Symbols used in the analysis are as follows:

P_A, P_F, P_C are the load of the active block and the frictional and cohesive zones of the passive block respectively.

$\bar{c}_I, \bar{c}_O$ are the cohesions of the inner and outer side of the active block respectively.

l_I, l_O are the shear failure lengths of the inner and outer side of the active block respectively.

l_F, l_C are the lengths of the frictional strength zones and the cohesive strength zones of the passive block failure surface respectively.

l_B is the length of the passive block failure surface and is equal to the sum of the lengths of frictional strength and cohesive strength zones ($l_B = l_F + l_C$).

β_I, β_O are the shear failure surface angles at the inner and outer sides of the active block respectively (assumed to be 45°).

R_P is the reaction of the passive block applied to the active block.

ϕ_{avI}, ϕ_{avO} are the average internal friction angles along the shear failure surfaces at the inner and outer side of the active block respectively.

ϖ is the dip angle of the strata.

In Chapters 2 and 3 it was mentioned that layers in the slope profile change in thickness along the undulated strata formation. For this reason, it is expected that they could have different thicknesses on opposite block sides, which means that the value of the average cohesion and friction angle will be slightly different. This level of detail is probably not appropriate in the model, so an average strata thickness is used, as shown in Figure 5.10.

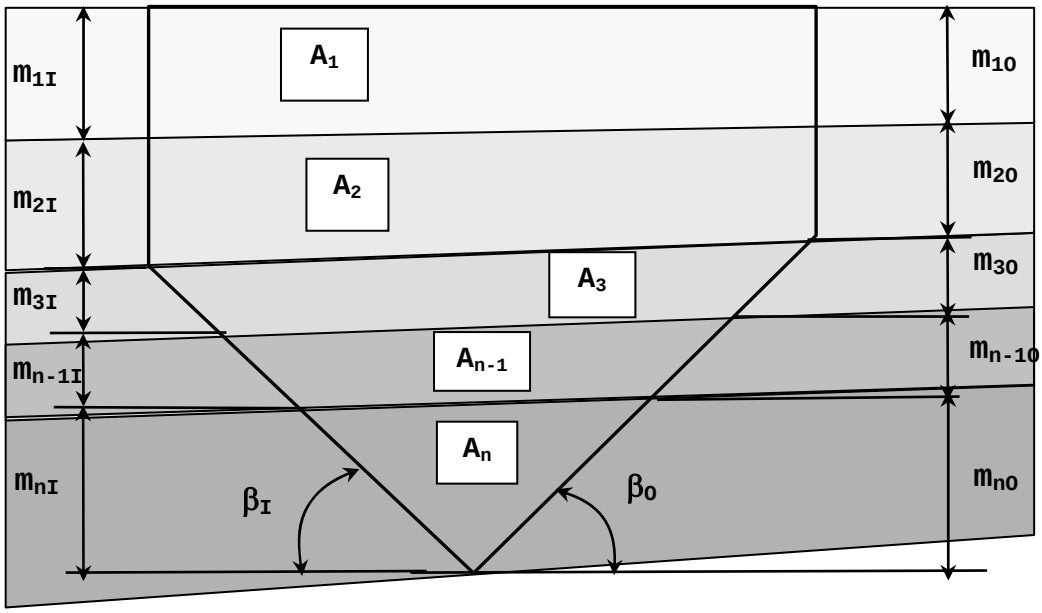

Figure 5.10

Active block, composed of different layers at average thicknesses

The average friction angle along each surface in a multi-layered medium can be expressed as the weighted average:

$$\phi_{ave} = \frac{\sum_{i=1}^{n} m_i \phi_i}{\sum_{i=1}^{n} m_i} \qquad (5.2)$$

where m_i is the layer thickness of the i^{th} layer and ϕ_i is the frictional angle of the i^{th} layer.

From the discussion in Section 5.3 and the assumptions made in Section 5.4, the shear failure surfaces are anticipated to dip at 45° to the horizontal. The tensile fracture depth has been estimated from the model, and is assumed equal to the tensile zone depth, shown in Figure 5.9. The average cohesion is calculated along the shear failure surfaces of the active block sides as the weighted average:

$$C_{ave} = \frac{\sum_{i=1}^{n} m_i C_i}{\sum_{i=1}^{n} m_i} \qquad (5.3)$$

where m_i is the failure surface length in the i^{th} layer and C_i is the cohesion of the layer intersected by the active block shear failure surface.

The active block weight for unit thickness is calculated as:

$$P_A = g \sum_{i=1}^{n} \rho_i A_i \qquad (5.4)$$

where A_i is the layer volume in the active block-profile, ρ_i is the layer density, and g is the acceleration due to gravity.

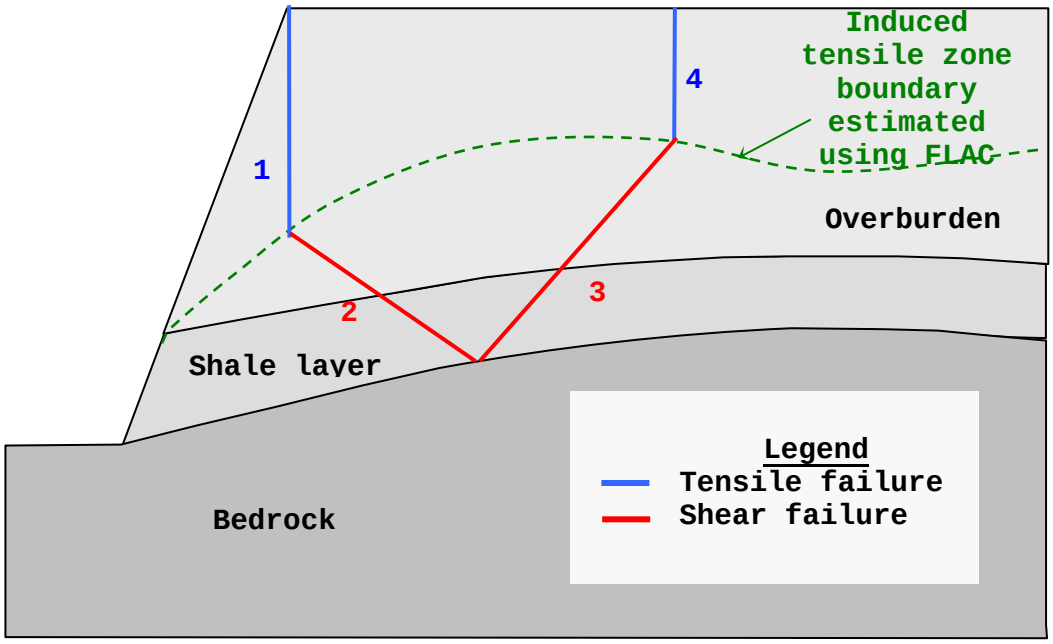

Figure 5.11

Active block construction sequence with the proposed failure types in the profile

The active block construction order (Figure 5.11) is as follows:

1. From the ground surface, at the crest of the slope, a vertical tensile fracture is drawn to a length equal to the depth of the calculated induced tensile horizontal stress zone (this is the area where tension fractures are most commonly seen).
2. A shear failure surface is drawn from the end of the induced tensile fracture downward to intersect the bottom shale contact surface at an angle of 45° to the horizontal in a direction toward the solid. This is the outer shear surface.

3. From this point, the line of the inner shear surface of the active block is drawn upward (toward the solid) to the bottom of the tensile zone at an angle of 45° to the horizontal.
4. The second vertical tensile fracture of the active block is drawn from the end of the shear failure line to the ground surface. This is the second vertical tensile crack, which would be encouraged to form because of small shear movements on the inner shear surface, and the fact that the presence of the slope has induced tensile horizontal stress below surface.

This construction is not intended to represent the sequence of development of these fractures as there is still insufficient evidence to determine exactly how the failure surfaces do grow within the slope. Once all these fractures are developed and connected, the formation of the active block is complete.

5.5.1 Calculation of the forces applied from the passive block to the failure surface

As was mentioned earlier, we have two zones along the failure surface at the passive block base, namely frictional and cohesive zones. These two zones have different shear strengths, which have to be taken into account when the resistance force developed by the passive block is computed. The passive block weight calculation is the same as for the active block.

Resisting forces at the base of the passive block are formed by the frictional strength along the failure

surface due to the block weight and the cohesive and frictional strength of that portion of the contact surface that has not yet yielded in shear. Driving forces are formed by the tangential component of the weight along the same surface. Hence, these forces can be expressed as:

$$P_F^N = P_F \cos\varpi \tag{5.5a}$$

and

$$P_F^{dr} = P_F^T = P_F \sin\varpi \tag{5.5b}$$

where ϖ is an average inclination angle of the failure surface, P_F is the passive block load above frictional zone, and P_F^N and P_F^T are the normal and tangential components respectively. The resisting force along the frictional zone will have the form:

$$P_F^{res} = P_F^N \tan\phi_E = P_F \cos\varpi \tan\phi_E \tag{5.6}$$

where ϕ_E is the frictional angle along the bedding.

Similar to the frictional zone, normal and tangential load components in the cohesive zone of the passive block can be calculated with Equation 5.7. Then the resisting and tangential forces to the failure surface will have the form:

$$P_C^{res} = c_B l_B + P_C^N \tan\phi_B = c_B l_B + P_C \cos\varpi \tan\phi_E \tag{5.7a}$$

and

$$P_C^{dr} = P_C \sin\varpi_C \tag{5.7b}$$

respectively.

5.6.2 Calculation of active block forces

Figure 5.9 shows that the rock mass rests on two potential failure surfaces: the shale-middle coal seam contact, and the active block inner shear failure surface. Blocky-type failure is only possible if an outer slip surface develops and an estimate of the overall safety factor of the system is the weighted average of the three safety factors, taking into account the lengths of the respective failure surfaces.

Active block movement is only possible if the reaction force from the passive block fulfils the Mohr-Coulomb failure criterion with the parameters for the internal slip surface – cohesion c, and friction angle ϕ, along the length l. Figure 5.12 shows the detail of the outer shear failure surface together with the passive block reaction force (R) acting on the surface.

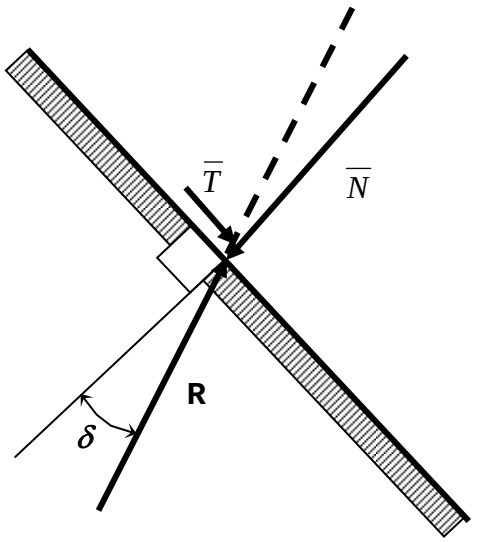

Figure 5.12
Detail of internal shear surface

From Figure 5.12 we can write

$$\overline{T}_{max} = \overline{N}\tan\phi + cl \tag{5.8}$$

If we take into account the definition for safety factor

$$FOS = \left| \frac{\text{maximum shear resistance}}{\text{applied shear stress}} \right| \tag{5.9}$$

Then we can write

$$FOS = \frac{\overline{S}_{max}}{\overline{S}} = \frac{\overline{N}\tan\phi}{\overline{T}} + \frac{cl}{\overline{T}} \tag{5.10}$$

From Figure 5.12 and Equation 5.10 we have

$$\tan\delta = \frac{\overline{T}}{\overline{N}} = \frac{1}{FOS}\left(\tan\phi + \frac{cl}{\overline{N}}\right) \tag{5.11}$$

and

$$\overline{N} = R\cos\delta \tag{5.12}$$

If we combine Equations 5.11 and 5.12 and accept FOS=1, which means that the internal slip surface is at the point of slipping, then we will have

$$\tan\delta = \tan\phi + \frac{cl}{R\cos\delta} \tag{5.13}$$

The angle of internal friction in Equation 5.13 has to satisfy the condition in Equation 5.14 if it is to have a real solution (see Appendix A1.4):

$$\phi \geq \sec^{-1}\left(\frac{cl}{R}\right) \tag{5.14}$$

From Equation 5.14 we can see that under worst-case conditions, $\phi = 0^{\circ}$ if $\frac{cl}{R} = \infty$, which is only possible if $R = 0$, and both $c \neq 0$ and $l \neq 0$. In the case of $l = 0$, we should have a tensile fracture from the surface to the failure surface. Kovari and Fritz (1978) accepted the worst-case scenario in their polygonal model, which gives the angle of reaction forces as equal to the angle of internal friction ($\delta = \phi$).

The following equations can be applied for the active block load distribution along the two shear failure surfaces that form the wedge structure:

$$P_{AO} = \frac{P_A}{2}\left(1 + \sin \varpi_A\right) \tag{5.15}$$

and

$$P_{AI} = \frac{P_A}{2}\left(1 - \sin \varpi_A\right) \tag{5.16}$$

for the outer and inner shear failure surfaces respectively, where P_A is the weight of the active block and ϖ_A is the layer inclination angle at the block wedge.

5.5.3 Calculation of the pore water forces

Figure 5.13 shows the same slope profile as shown in Figure 5.9, with points defining the block boundaries. Let us first calculate the pore-water pressure along the line “CD”. The earlier-calculated induced vertical

tensile fracture depth (z) and a phreatic surface, (z_{WT}), above the tensile fracture depth are indicated.

Therefore, the pore-water pressure at point "D" in Figure 5.14 is equal to:

$$\sigma_w^D = \gamma_w z_{WT} \tag{5.17}$$

where γ_w is the unit weight of water and z_{WT} is the surface tensile fracture depth below the phreatic surface.

The total force acting along the surface vertical tensile fracture at the active block outer side is equal to

$$V_w^{CD} = \frac{\gamma_w z_{WT}^2}{2} \tag{5.18}$$

Let us calculate the pore-water pressure along the line DE. As a first step, let us define pore-water pressure along the line DA. For this purpose we assume zero pore-water pressure at point D. We also have zero pressure at point A at the slope toe position. Hence, we assume that, in the middle of the span between these two points (point I), we will have the highest pore-water pressure value that will be equal to

$$\sigma_w^I = \frac{\gamma_w z_w^{DA}}{2} \tag{5.19}$$

where z_w^{DA} is the difference between depths of points D and A. Now we cam draw a stress diagram (ADJ) between the points A and D.

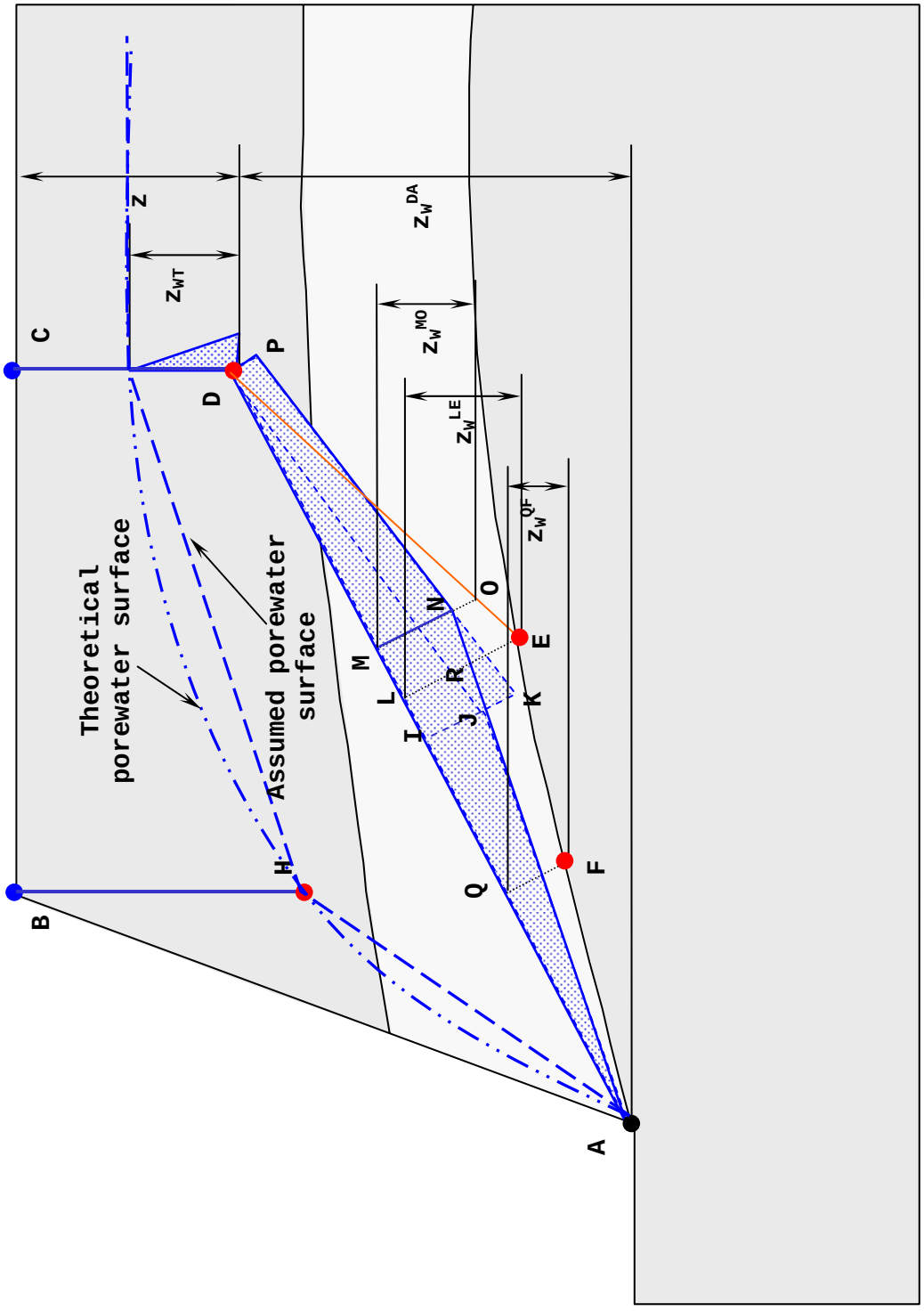

Figure 5.13

Scheme for pore-water pressure calculation on the passive and active block boundaries

From Equation 5.13, we have pore-water pressure at point D. So let us draw the line DP, equal to the pore-water pressure at point D normal to the line AD and add the same stress magnitude at point I as adding stress JK. Now our stress diagram takes a new form (AJKPD), which is unrealistic because of the step AJK. As the point I is in the middle of AD, then half of the stress JK can be added to the portion AI and the other half to the portion ID. Hence, we have a new stress equal to

$$\sigma_w^I = 0.5\gamma_w\left(z_w^{DA} + z_{wt}\right) \tag{5.20}$$

which is equal to the line MN in our stress diagram. Then let us move our stress magnitude MN toward point D until it intersects the stress line KP. This position is shown in Figure 5.13. Now we have a new stress diagram (ANPD), which presents pore-water pressure distribution along the line AD.

Let us now calculate the pore-water pressure at point E. For this reason, let us make its orthogonal projection to the line AD, which is point L, which has pressure with the magnitude LR. Therefore, the pore pressure at point E will have the magnitude

$$\sigma_w^E = \sigma_w^L + \gamma_w z_w^{LE} \tag{5.21}$$

where z_w^{LE} is the depth difference between the points L and E. This pressure is realistic because point E is slightly deeper than point L.

To find the point where we have maximum pore-water pressure along the outer shear failure surface we define point O, whose orthogonal projection to the line

AD is point M. With a high degree of approximation we can say that the pore-water pressure at point O is equal to

$$\sigma_w^O = \sigma_w^M + \gamma_w z_w^{MO}. \quad (5.22)$$

It is now easy to construct a pore-water pressure diagram along the line of the inner shear failure surface (HE) because we have calculated the pore-water pressure at point E (Equation 5.21) and have assumed zero water pressure at point H. This assumption is based on the close point position to the two free surfaces AB and BC.

Pore-water pressure at point F follows the same order as for point E (Equations 5.21 and 5.22):

$$\sigma_w^F = \sigma_w^Q + \gamma_w z_w^{QF} \quad (5.23)$$

where σ_w^Q is the pore-water pressure magnitude at point Q and z_w^{QF} is the depth difference between the points Q and F.

Now we are in position to draw the pore-water pressure diagrams along the active block failure surfaces and the passive block failure surfaces. Figure 5.14 shows pore-water pressure diagrams and resultant forces V_{CD}, U_O, U_I, U_C and U_F acting along the failure surface of the vertical tensile fracture, the active block outer and inner shear failure surfaces, and the cohesive and frictional lengths respectively of the passive block base. The figure also shows the calculated pore-water pressures σ_w^D, σ_w^E, σ_w^0 and σ_w^F at points D, E, O and F

respectively. According to the pore-water pressure diagrams, calculated resultant forces have the following magnitudes:

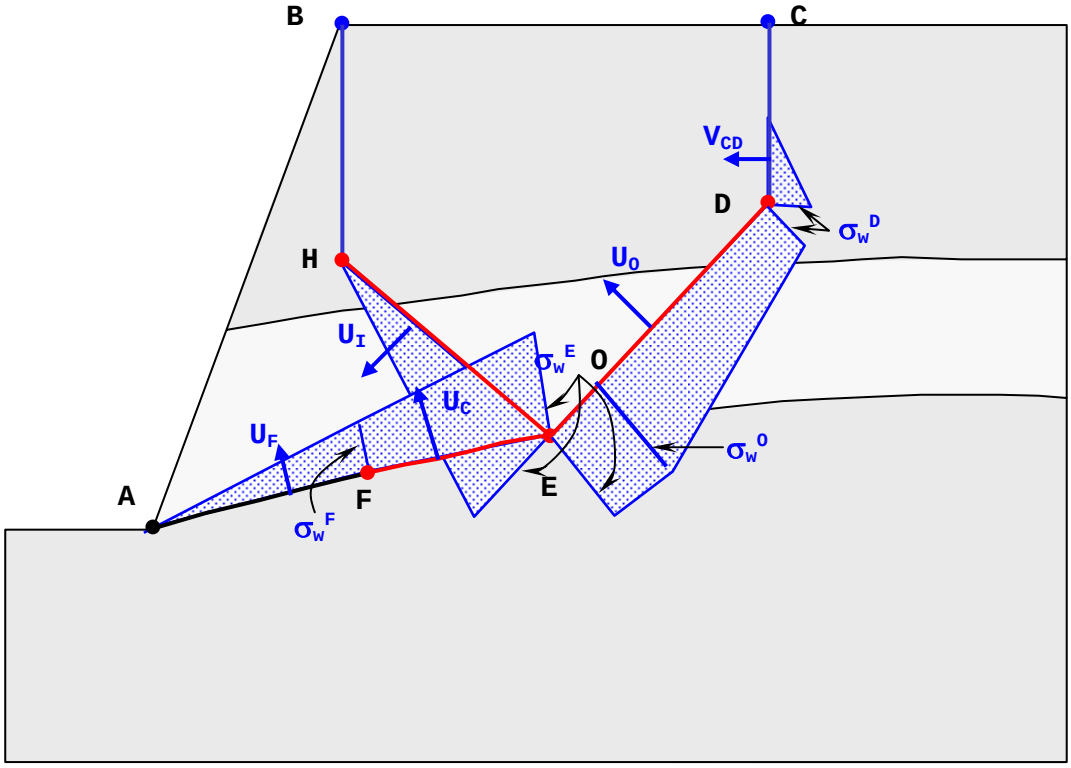

Figure 5.14

Pore-water pressure diagrams

$$U_O = \frac{l_{DO}\left(\sigma_w^D + \sigma_w^O\right)}{2} + \frac{l_{EO}\left(\sigma_w^O + \sigma_w^E\right)}{2} \qquad (5.24)$$

$$U_I = \frac{l_{EH}\,\sigma_w^E}{2} \qquad (5.25)$$

$$U_C = \frac{l_{EF}\left(\sigma_w^E + \sigma_w^F\right)}{2} \qquad (5.26)$$

$$U_F = \frac{l_{AF}\,\sigma_w^F}{2} \qquad (5.27)$$

where l_{DO}, l_{EO}, l_{EH}, l_{EF} and l_{AF} are span lengths between points DO, EO, EH, EF and AF respectively.

Similar pore-water pressure analysis was undertaken by Hoek (1986) in his lecture at the Santiago Technical University (Chapter 7 “A slope stability problems in Hong Kong”).

5.5.4 Criterion for the existence of the inner shear surface

At the inner shear surface we have the combined action of two forces. The first force takes into account the sum of driving and resisting forces (with the signs “-” and “+” respectively) along the potential failure surface of the passive block base, expressed as

$$R_P = P_F^{res} + P_C^{res} - P_F^{dr} - P_C^{dr} \qquad (5.28)$$

and, secondly, the corresponding active block load.

Hence, we could have two directions of the passive block reaction force (Equation 5.28): the first one is when the sum is negative (Figure 5.18a) and the second, when the sum is positive (Figure 5.15b). Acceptance of the reaction force inclination angle ($\delta = \phi$), allows us to use only cohesive strength along the inner shear failure surface. We can transfer the normal to the inner surface component of the passive block reaction force (R_P), to the outer failure surface with the corresponding inclination angle.

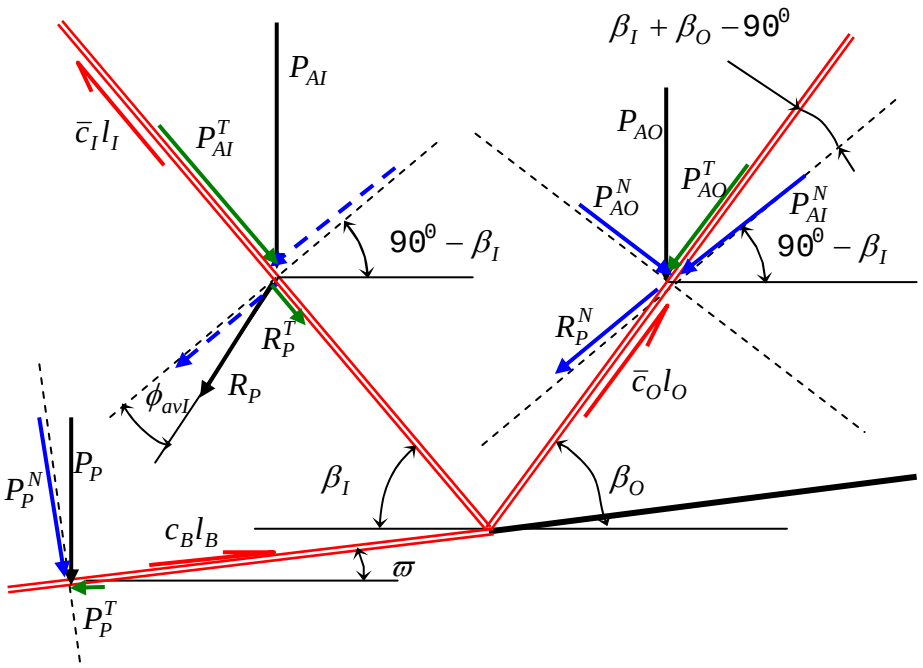

Figure 5.15a

Passive block reaction force R_P acting approximately co-directional to the active block load at the inner shear failure surface

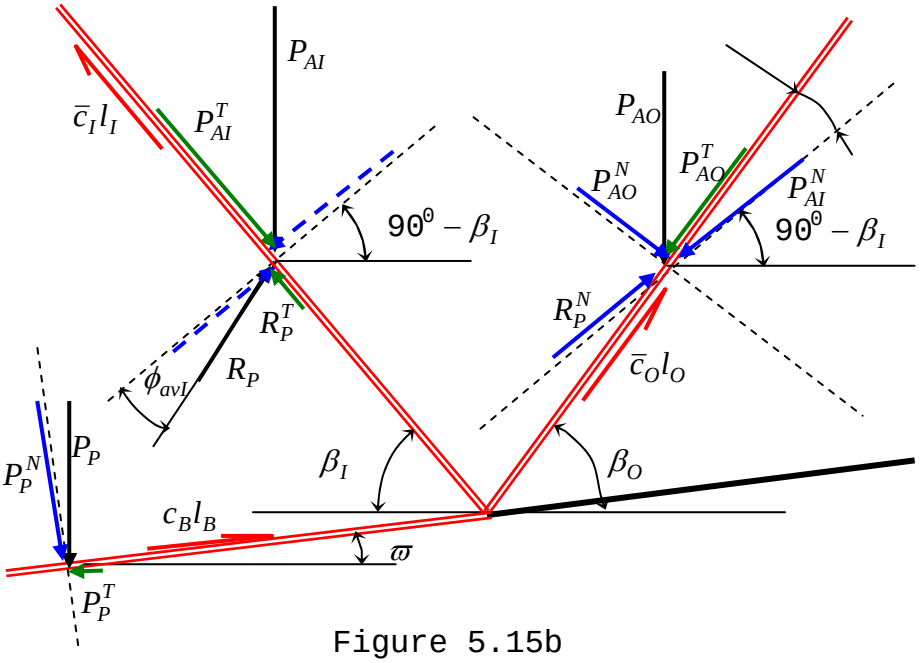

Figure 5.15b

Passive block reaction force R_P acting opposite to the active block load at the inner shear failure surface

In the first case (Figure 5.15a), the normal components on the shear surface under the passive block and the corresponding active block weight (R_P^N and P_{AI}^N) are approximately co-directional, which increases the driving forces of the active block outer shear failure surface and might lead to failure. Hence the active block inner failure surface will have only cohesive strength.

In the second case (Figure 5.15b) we have reaction force, acting opposite to the force of the active block load. Tangential (to the inner shear surface) components of the reaction force and the corresponding active block load are in opposite directions, which will decrease the total driving effect.

Using the above discussion and assumption that $\delta = \phi$ eliminates frictional resistance of the inner failure surface, we can use Equation 5.10 to define the criterion for the existence of the inner shear failure surface, which has the form:

$$\eta = \frac{cl}{P_{AI}^T - R_P^T} \tag{5.29}$$

If we take into account Equations 5.16 and 5.17 and the relationships

$$P_{AI}^T = P_{AI}\, \boldsymbol{sin}\, \beta_I \tag{5.30}$$

$$R_P^T = R_P\, \boldsymbol{sin}\, \phi_I, \tag{5.31}$$

then Equation 5.29 can be rewritten as

$$\eta = FOS_I = \frac{\bar{c}_I l_I - U_I \tan\phi_{avI}}{\frac{P_A(1+\sin\varpi_A)\sin\beta_I}{2} - R_P \sin\phi_{avI}}, \quad (5.32)$$

which is a criterion for the existence of the inner shear failure surface and the surface's factor of safety.

If the shear fracture criterion (η) from Equation 5.32 is higher than 1.3, the inner shear failure surface will not form. Therefore, we will have conditions for other failure types (such as multi planar or polygonal) but not for thrust failure. If the criterion is lower than 1.3, we have to anticipate shear failure at the inner surface and, from there, blocky-type failure.

5.5.5 Calculation of the outer shear failure surface factor of safety

As was discussed earlier, the components normal to the inner failure surface of the corresponding active block load and the passive block reaction force are transferred to the outer shear surface. Then their combined action along the outer surface can be expressed as (Figure 5.18):

$$\bar{R} = \frac{P_A}{2}(1+\sin\varpi_A)\cos\beta_I - R_P \cos\phi_{avI} \quad (5.33)$$

Therefore, the outer shear failure surface will have a factor of safety equal to

$$FOS_O = \frac{\bar{c}_O l_O + \left[\bar{R}\,\sin\left(\beta_I + \beta_O - 90^0\right) + \frac{P_A}{2}\left(1 - \sin\varpi_A\right)\cos\beta_O - U_O - V_{CD}\sin\beta_O \right]\tan\phi_{avO}}{\bar{R}\cos\left(\beta_I + \beta_O - 90^0\right) + \frac{P_A}{2}\left(1 - \sin\varpi_A\right)\sin\beta_O + V_{CD}\cos\beta_O} \quad (5.34)$$

In term of Section 5.3, Equation 5.34 can be further simplified as:

$$FOS_O = \frac{\bar{c}_O l_O + \left[\frac{P_A}{2}\left(1 - \sin\varpi_A\right)\cos\beta_O - U_O - V_{CD}\sin\beta_O \right]\tan\phi_{avO}}{\bar{R} + \frac{P_A}{2}\left(1 - \sin\varpi_A\right)\sin\beta_O + V_{CD}\cos\beta_O} \quad (5.35)$$

5.6.6 Calculation of the basal failure surface factor of safety

The basal surface safety factor presents the balance of already calculated driving and resisting forces along the contact surface in the passive block base (see Figure 5.12), and has the form:

$$FOS_B = \frac{P_F\cos\varpi_F\tan\phi_B + \left(c_B l_C + P_C\cos\varpi_C\tan\phi_B\right) - \left(U_C + U_F\right)\tan\phi_B}{P_F\sin\varpi_F + P_C\sin\varpi_C} \quad (5.36)$$

where ϕ_B is the friction angle along the sedimentary layer and ϖ_F and ϖ_C are the layer inclination angles along the frictional zone and cohesive zone of the passive block base.

5.6.7 Slope stability safety factor

The failure surface lengths (l_I,l_O and l_B - Figure 5.12) vary, and depend on slope angle, layer inclination, layer thickness, and rock properties. To avoid overestimating the influence of the shortest failure surface on the entire slope stability, a weighted function of calculated safety factors should be used. Hence, we have the following weighted average equation for calculation of the entire slope stability factor of safety from the individual failure surface factors of safety and their respective lengths:

$$FOS = \frac{FOS_I l_I + FOS_O l_O + FOS_B l_B}{l_I + l_O + l_B} \qquad (5.37)$$

5.6 CONCLUSION

A simple active-passive block formation mechanism based on the Mohr-Coulomb failure criterion and fracture mechanics has been developed, and will now be applied to the observed failures discussed in Chapter 1.